COMBINED EFFORT OF REFLECTANCE SPECTROSCOPY AND BVRI PHOTOMETRY IN THE FIELD OF SPACE DEBRIS CHARACTERIZATION

Matej Zigo, Danica Žilková, Jiří Šilha, Juraj Tóth, and Pavol Matlovič

Faculty of Mathematics, Physics and Informatics, Comenius University, Mlynska dolina, Bratislava, Slovakia

ABSTRACT

The reflectance spectroscopy and BVRI photometry are two widely used procedures in many different fields of astronomy. Thanks to these observation techniques we categorize objects into groups according to similarities in surface properties and characteristics, improve our knowledge about the density of specific materials on-orbit, identify specific spectral features, related to certain materials in comparison to laboratory samples and find evidence of material "reddening" caused by the space-weathering or aging effects.

The photometric measurements, acquired by the AGO70 telescope, are capable of recognition and processing of the diffuse part of the reflection, while the reflectance spectroscopy with the AMOS-Spec cameras capture specular reflections. Both methods are based on the capturing and processing of the incoming sunlight reflected by the object's surface, which enables us to reconnect these methods again and use them for the cross-calibration. In this article we will present the instruments and methods of the data processing, as well as the example results.

Keywords: Characterization; BVRI photometry; Reflectance spectroscopy.

1. INTRODUCTION

The main motivation for any spectroscopic and photometric measurements is the object characterization and categorization according to its surface properties. General objective is to be able to describe the complex composition of spacecrafts and identify distinctive features and materials, which are dominantly reflective in actual line of sight. The detailed designation of the surface properties can help us to properly select the potential approach to active debris removal missions, correlate the fragments with their ancestors and determine the possible reasons of the fragment formation. Resolving these problems is crucial to maintain the turbulent space debris population and decrease the risks of new fragment formation.

From the definition, space debris are inactive objects after the passivation or accidental loss of communication, so the objects are without any function. These objects do not emit any light and that is why the whole measured light belongs to the reflected sunlight. This assumption means that any measured changes in the spectrum of the visible light or in the color indices will be caused by the surface properties and materials of the target body.

Object characterization can be performed through the relative comparison to the known populations with measured spectra or estimated color indices. This method provides the categorization, possibility for long-term monitoring of the material weathering, and additional argument in the correlation of the debris fragment and parent bodies. Another approach is the correlation of the spectral shape or color indices with the laboratory based measurements. Generally, object characterization represents an estimate of the surface properties, such as the surface material colors, roughness, albedo etc..

The Faculty of Mathematics, Physics and Informatics of Comenius University in Bratislava (FMPI), is simultaneously operating two different instruments, which are used for our research. The very first one is the 70 centimeter telescope AGO70, installed at the Astronomical and Geophysical Observatory (AGO) in Modra. Another instrument is the worldwide All-Sky Meteor Trajectory System (AMOS) network. Instrumentation, acquired data and data processing will be introduced and demonstrated in this article.

2. INSTRUMENTATION

2.1. AGO70

The photometric data in this work was provided by our optical passive system, hereafter AGO70 (Figure 1) [1], which has been installed at AGO (Minor Planet Center code 118) in September 2016. AGO70 is operated by FMPI. Its observations are primarily dedicated to the space debris research and Space Surveillance and Tracking (SST). We distinguish three major observation programs at AGO70 - the astrometry to support SST, instrumental photometry to characterize the debris attitude

Proc. 8th European Conference on Space Debris (virtual), Darmstadt, Germany, 20–23 April 2021, published by the ESA Space Debris Office
Ed. T. Flohrer, S. Lemmens & F. Schmitz, (http://conference.sdo.esoc.esa.int, May 2021)

states, and BVRI photometry to characterize the debris surface properties and hence identify the object's origin.

Figure 1: AGO70 in its cupola at Astronomical and Geophysical Observatory in Modra, Slovakia.

Parameters of the AGO70 are listed in Table 1. The presented system is a Newton design telescope with a very thin parabolic mirror with diameter 700 mm from Alluna optics supported by gravity actuator. The focal length of the system is 2962.0 mm. The CCD sensor is the FLI Proline PL1001 Grade 1 CCD camera with 1024 x1024 pixels and 24m pixel size which results in a field-of-view (FoV) of 28.5 $'x$ 28.5 $'$ and iFOV of 1.67 $''/pixel$. AGO70 is equipped with a filter wheel with Johnson-Cousins filters BVR$_c$I$_c$. In 2020, the AGO70 was upgraded to be able to track objects up to the angular velocity of approximately 2 deg/s [1].

Table 1: AGO70 definition parameters. Credit: [2]

Operator	FMPI
Telescope	AGO70
Telescope design	Newton
Mount	Equatorial (Open fork)
CCD Camera	FLI-ProLine KAF-1001E
Dimension	1024x1024
Primary Mirror [mm]	700
Focal length [mm]	2962.0
Focal ratio	f/4.2
FoV [arc-min]	28.5 x 28.5
iFoV [arc-sec/px]	1.67

2.2. AMOS network

All-Sky Meteor Orbit System (AMOS) is fully-automated and remotely controlled system of cameras for detection and orbit determination of meteors. This system has been developed and is operated by the FMPI and the system currently consists of two major parts, the all-sky AMOS-Cam and AMOS-Spec/AMOS-Spec-HR [3]. The network is world-wide distributed, with locations depicted in Figure 2, namely with stations in Slovakia, Canary Islands, Chile and Hawaii. Further expansion of the network is planned in central and eastern Slovakia as well as in South Africa and Australia.

Wide distribution secures large sky coverage, Northern and Southern hemispheres observed simultaneously, and the trigonometry to accurately determine the atmospheric trajectory, which then leads to the pre-atmospheric heliocentric orbit and eventually estimates whether the meteor belonged to a certain meteor shower or to a sporadic background.

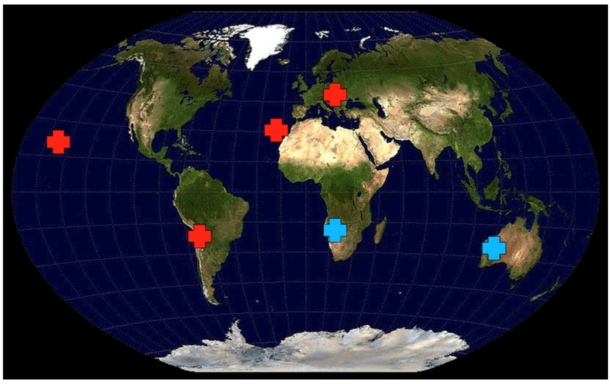

Figure 2: World-wide distribution of AMOS meteor network.

AMOS-Cam; global system of cameras monitoring meteor activity around the world. The AMOS-Cam camera consists of a fish-eye lens, image intensifier, projected lens and digital camera, operating computer with harddrive, weatherproof enclosure, temperature, humidity and light sensors. Its primary focus is to capture meteors however during the nominal operation detection of other objects, such as satellites and orbital debris, occurs on regular basis.

Within the video system two types of spectral cameras are installed in AMOS network, AMOS-Spec and AMOS-Spec-HR [4]. AMOS-Spec is only installed at AGO, while AMOS-Spec HR is installed world-wide. First attempt to perform spectroscopic reduction of space debris recordings was evaluated on AMOS-Spec data. All the extraction processes and results were presented at The 1st International Orbital Debris Conference, at NASA, Houston, USA; [5]. However the initial data were mostly experimental and were vastly improved since. Mainly the research had shifted from AMOS-Spec to world-wide distributed AMOS-Spec-HR. It was concluded that AMOS-Spec-HR is better choice to follow with the research since it allows us to extend our database to three more locations; La Palma and Tenerife in Canary Islands, and San Pedro in Chile. Furthermore high resolution spectrograph provides recordings with advance quality and makes our processing method; mainly the conversion from pixels to wavelengths, more accessible.

AMOS-Spec-HR; a new higher resolution spectrograph, with display component of these spectrographs based on a 6 mm f/3.5 lens, high definition digital Point Grey camera providing 60 × 45 degrees FOV with a resolution of 1.76 arc-min/pixel and frame of 15 fps. The applied 1000 grooves/mm holographic diffraction grating results in spectral resolution of 0.5 nm/pixel. The typical limiting magnitude of the system is approx. +3 for meteors and -1.5 for meteor spectra.

3. CHARACTERIZATION THROUGH THE COLOR INDICES

The multi-band photometry can be understood as the low-resolution spectroscopy. It is a common astronomical methodology, which serves for the categorization and characterization of the objects. Thanks to its simplicity and lower requirements on the scientific instruments, it is an ideal method for fast and deeper look into the nature of the observation targets.

3.1. Photometric reduction

To obtain transformation into the standard magnitude system we use the general transformation equation which considers effect of telescope's zero point (ZP), atmospheric extinction (k) and color term (t_f) (Eq. 1):

$$M - m = k \cdot X - ZP - t_f \cdot (CI), \qquad (1)$$

where M represents the calculated standard magnitude, m is the measured instrumental magnitude, X is the air-mass calculated as secant of the zenith angle and CI stands for selected color index. Eq. 1 is a linear equation with three unknown parameters (k, X, t_f) [6].

To estimate the unknown parameters in Eq.1 we observe star fields from the Landolt's catalogue of the standard solar analogs located near the celestial equator [7, 8]. Fields of the standard stars are selected to reliably satisfy the interval of the air-mass and intensity air-mass and intensity values obtained for the debris objects. The instrumental intensities of the standard stars are fitted using the least squares method. Thanks to this fit we are able to compute the transformation coefficients together with their uncertainties. The input instrumental photometric uncertainty, estimated using the standard CCD photometric noise estimation relation [9], is then propagated through our calculations.

3.2. Color indices and rotational phase dependence

After the reduction the photometric solution is used to transform the targets' instrumental magnitudes and the color indices are estimated as a difference of the averaged standard magnitude in different passbands. The very first look on the object's surface material character is offered by the material groups in the BVRI diagram defined in the article [10]. These groups were defined using the correlation of the objects' reflectance spectra and laboratory measured spectra of the solar cell (I), gold (II) and silver (III) samples and the color indices had been estimated (Figure3). The target's position in the BVRI diagram represents the color of the dominantly reflective component from the diffuse reflection of the surface in our line of sight.

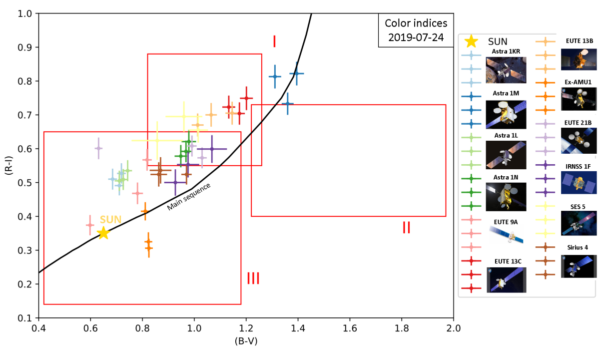

Figure 3: Example of the observational night results for the stable targets. Each point represents the average of the three measurements and objects were measured under different phase angles.

During the planning of the photometric observations of the space debris targets, the apparent rotational period of the objects has to be taken into account to be able to extract the representative average color indices. For a stable object, only a few measurements are necessary to obtain the averaged color indices. To remove effects of the phase angle changes, the observation is repeated and results are averaged through the night. On the other hand, to obtain average color indices for the rotating objects, the whole rotational period has to be measured and averaged. For the planning process we use the FMPI's light curve catalog of the space debris objects [2].

Besides the representation by only one point, we perform the processing of the color light curves, so light curves acquired in four different passbands. This technique is performed using the light curve processing pipeline developed at the FMPI [2]. In the first step, the instrumental light curves are extracted and transformed into the standard system of the magnitudes separately. Afterward, the apparent rotational period is estimated simultaneously for all passbands using the Lomb-Scargle method and confirmed and corrected using the phase-dispersion minimization. Estimated apparent rotational period is then used to fold the light curves into the rotational phase functions i.e. relations between rotational phase and targets brightness [1]. These functions are then fitted using Fourier series to obtain the mathematical expression along the whole phase and the rotational phase dependencies of the color indices are estimated. Thanks to this method we obtain the target's path in the BVRI diagram along the rotational phase, which is expected to be the closed curve representing the change of the object's surface color during one rotational period. This methodology is very sensitive firstly because of the uncertainties in the apparent rotational period estimation and also for the photometric uncertainties. In both cases, lower data and methodology quality can result in the strong changes of the output BVRI paths. Another strong factor is the phase angle. The change of the brightness, in the photometric passbands under specific phase angle, results in the significantly different shape of the BVRI path.

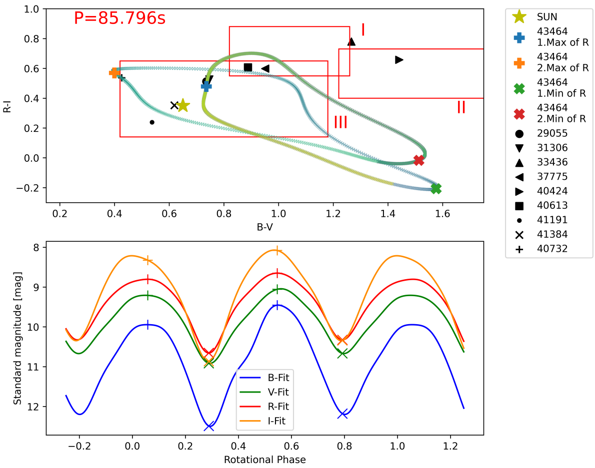

Figure 4: Plot above consists of BVRI path of the Falcon 9 (NORAD 43464) with marked points related to the local extremes of R-filter Fourier series, material groups [10] and selected stable GEO satellites. Bottom image shows the alignment of the color rotational phase functions in the interval $((0,1) \pm 0.2) \cdot 2\pi$ for demonstration of the continuous character of the curves. This measurement was done under the phase angle $\phi \approx 30\ deg$.

These closed curves can be used for the interpretation of the reflecting materials and their properties, as well as for the identification of the specific features on the surface of the target. In the Figure 4 can be seen the BVRI path of the Falcon-9 rocket body. The marked extremes show that the maximal reflection related to the white painted coat has more blue color than the metallic bases. Moreover, the reflections of the bases differs, the stronger red color of the first minimum is probably related to the base with the rocket nozzle, which is expected to be affected by the fuel burning. Closer look into the material characterization can provide the laboratory measured samples of the commonly used materials in the space engineering and extended catalog of the color indices of different populations with known shapes and assumptions on the surface materials.

4. CHARACTERIZATION THROUGH THE REFLECTANCE SPECTRA

Refelctance spectroscopy, already widely used in asteroid classification, allows us to categorize objects into groups according to the similarities in their surface materials. The technique identifies specific features in the spectra which relate to different constituents and hereby presented research proposes its application into space debris domain. The work will be demonstrated on several real cases captured during nominal operation of AMOS spectral cameras.

4.1. Spectroscopic reduction

Radiation from the Sun travels towards the Earth, if it strikes an object in its way, it is reflected storing the information about the object's material. Radiation flux recorded by a detector on Earth is described by Equation 2.

$$Y(\lambda) = [X(\lambda)HA(\lambda) + T(\lambda)]HT(\lambda) \tag{2}$$

Where $X(\lambda)$ is the radiation flux from the Sun, $HA(\lambda)$ the transfer function of the object, $HT(\lambda)$ includes the transfer function of the Earth's atmosphere and of the optical instrument, and $T(\lambda)$ is the thermal infrared emission of the object. [11]. However spectroscopic reduction will be zoomed into the spectral regions (wavelengths of visible light) where the thermal emission is negligible in comparison with the reflected radiation, hence we restrict to the term 'reflectance spectroscopy'. Equation 2 reduces to 3 and the spectrum, i.e. the transfer function of the object, is given by dividing the recorded radiation flux by the radiation flux from the Sun and the transfer function of the Earth's atmosphere and optical instrument.

$$HA(\lambda) = \frac{Y(\lambda)}{X(\lambda)HT(\lambda)} \tag{3}$$

Data reduction process will be demonstrated on AMOS-Spec-HR space debris data, to be precise on the recording of SPOT 3 (NORAD 22823) satellite which appeared as a bright specular flash on 25th of August 2018 05:34:29.00 UTC on a camera in Tenerife, Canary Islands. AMOS data comes in form of short videos recording an event, these videos are loaded into ImageJ software [12] and processed. To obtain the best quality signal in the most consistent way image processing must come in the following stages:

1. Flip horizontally: make sure that the zero order and first order lay out is from left to right.

2. Stack for more intensity: if the spectrum appears in more than one frame and is faint consider stacking the frames to intensify the spectrum.

3. Background extraction: Subtract the medium image created from the frames outside of the recorded event.

4. Zero Order: it is important for future analysis to note down the pixel where the zero order occurs.

5. Measure the spectrum starting from the zero order.

Object identification is performed by astrometric measurements. Astrometric reduction is performed using tool UFOAnalyzer [13] and compared with the ephemerides calculated with the FMPI's internal tool SatEph [14] which is built based on the SGP4 model [15]. The software uses the Two-Line Elements (TLE) set obtained from the public catalogue [16] to calculate the exact position of the object for given observer and observation epoch. For hereby purposes it will serve as a main identification method.

Signal to noise ratio (SNR) was computed using Equation 4 to assess the quality of the recording. S is the total integrated signal from the object's measurement, n is the number of pixels within the aperture (when measuring spectra pixel per pixel $n = 1$), B is the mean measure of the background, T is the thermal signal collected by the pixel, respectively, and $(\sigma_R)^2$ is the readout noise for one pixel. In case of this type of spectroscopic measurements T and $(\sigma_R)^2$ can be neglected.

$$SNR = \frac{S}{\sqrt{S + n(B + T + (\sigma_R)^2)}} \tag{4}$$

Furthermore to compute the total noise Equation 5 is used.

$$\sigma = \frac{S}{SNR} \tag{5}$$

Once SNR and raw spectrum is extracted all the transformations the spectrum must subdue to output the reflectance spectra will follow. Noise will be computed along every step of the spectroscopic reduction throughout every transformation of the spectrum. *SatSpec.py* program was developed in python programming language to perform all the necessary spectral transformations.

Pixels to wavelengths are converted using regression polynomials. To perform such conversion, regression coefficients were derived from known meteor spectra emission lines. For each px_0 zero order - location where the specular flash occurs, set of coefficients is assigned and using Equation 6 pixels are converted into wavelengths.

$$wavelength = b + m_1(px_0)px + m_2(px_0)px^2 \tag{6}$$

Coefficients b, m_1 and m_2, illustrated in the Figure 5, are derived from meteor spectra and reversely tested on meteor spectra which is then compared with standard method of converting pixels to wavelengths by identifying meteor emission lines. The developed method proved to be effective with only few nanometers shift in wavelengths.

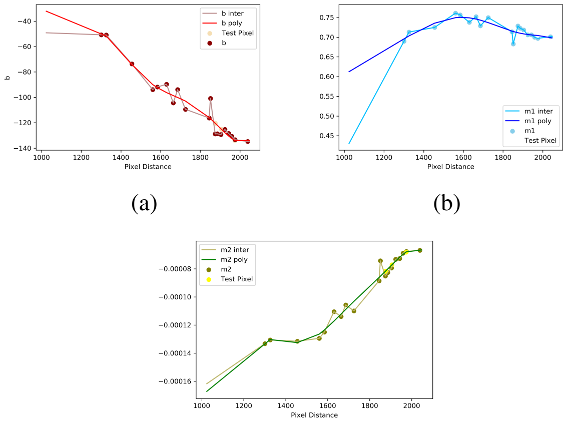

(a) (b) (c)

Figure 5: Estimated coefficients from the equation 6. 5a: b parameter; 5b: m_1 parameter; 5c: m_2 parameter;

Finally, the spectrum's zero order is cut off, it is normalized and converted into wavelengths according to the Figure 6. SNR is also printed out in this figure.

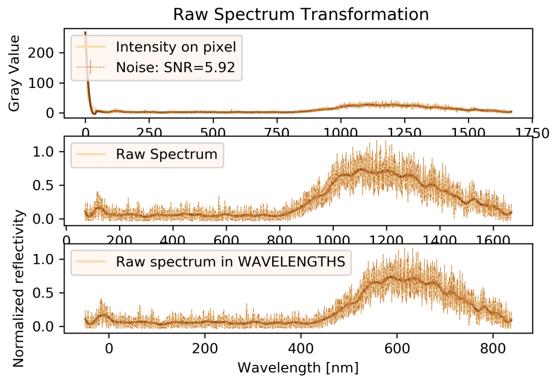

Figure 6: SPOT 3 raw spectrum conversion into wavelengths

Raw to reflectance spectrum is obtained via three transformations. The raw spectrum must be divided, according to the Equation 3, first by camera's spectral response curve, or sensitivity, secondly by the atmospheric extinction and finally by the solar spectrum. All three curves are in Figure 7.

The spectral sensitivity of the AMOS-Spec-HR system was determined using reference calibration lamps. Atmospheric extinction was extracted using the Tapas model [17]. This model is a free on-line service for the astronomical community, allowing the user to access a simulated atmospheric transmission for the specific observing conditions. Thirdly, to obtain the relative reflectance spectrum it is necessary to divide the spectrum by solar spectrum. In this case we have used 2000 ASTM Standard Extraterrestrial Spectrum E-490 in the wavelengths range of 300 – 1000 nm [18]. The reflectance spectrum of SPOT 3(93061A, 22823) is shown in Figure 8.

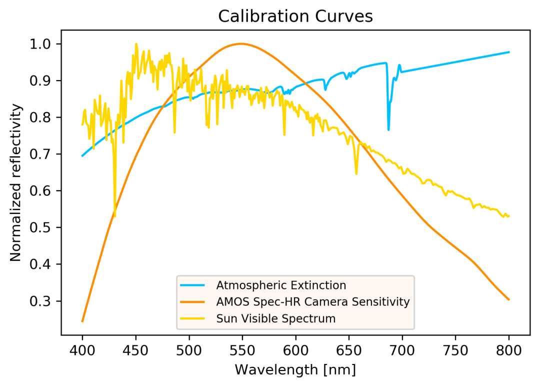

Figure 7: AMOS-Spec-HR spectral response curve - ORANGE. Atmospheric extinction for SPOT 3 on25th of August 2018, Tenerife - BLUE. 2000 ASTM Standard Extraterrestrial So-lar Spectrum - YELLOW.

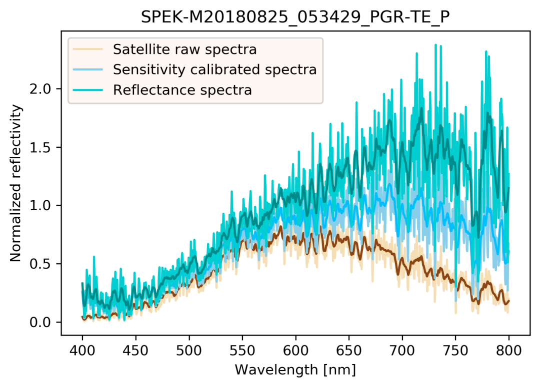

Figure 8: Reflectance spectrum - SPOT 3

Reflectance spectrum represents object's ability to reflect specific wavelengths according to the surface material. Since only few known materials are used in space missions, with proper laboratory documentation, comparing spectrum with laboratory data, material type is predicted. To analyze the spectral type of a reflectance spectrum Spearman rank-order correlation was used, a non-parametric measure of the monotonicity of the relationship between two data sets. Data is correlated with laboratory data [19]. To ensure the correct slope of each spectrum, lowess function is used to implement local linear estimate of the noisy data. In this way the signal noise will be suppressed and the output function will be smooth.

According to Figure 9, AMOS-Spec recording from 25th of August 2018, identified as the satellite SPOT 3 (93061A, 22823), and in the plot indicated by the green curve, has a coincidence of 99% with the laboratory spectrum of multi-layer insulation, in this case it corresponds to gold-copper color. Golden Multi-Layer Insulation (MLI) is thermal insulation composed of multiple layers of thin sheets. It is one of the main items of the spacecraft thermal design, primarily intended to reduce

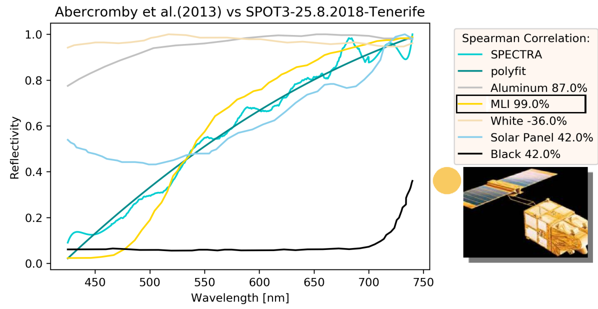

Figure 9: SPOT 3 correlation with laboratory data

heat loss. In this case it is defined by a golden color, with strong spectral feature peaking in the yellow-red wavelengths region of visible light. Although MLI exists also in the form of aluminized insulation, such color will not show the golden spectral features.

In the same manner as satellite SPOT 3 was processed and analyzed next 38 samples of space debris recorded by AMOS-Spec-HR were evaluated. Collecting the data attentive catalogue was created to note down all the spectral properties to select the best candidates which will represent the different material types. Mainly we were looking for MLI, solar panel and aluminium.

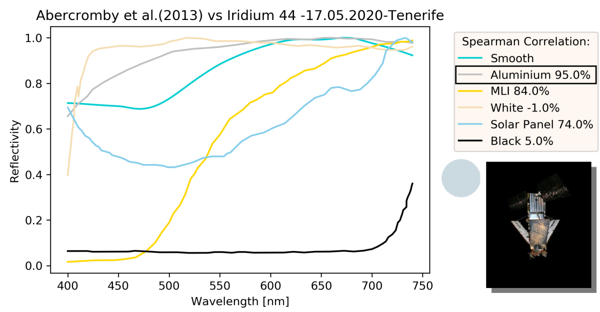

Figure 10: Iridium 44 correlation with laboratory data

Recording from 17th of May 2020, Figure 10, identified as Iridium 44 (97077B, 25078), corresponds to reflectance spectrum of aluminium by 95%. Aluminium is the most frequently used material in space missions, its reflectance spectrum resembles a perfect mirror with the curve almost completely straight.

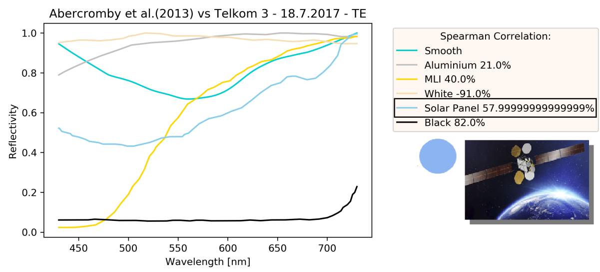

Figure 11: Telkom 3 correlation with laboratory data

Last type of space debris spectra we encountered, Telkom

3 (12044A, 38744), Figure 11, occurred on 18th of July 2017 and resembles solar panel spectra with 58% match. Solar panel spectra shows strong features at the beginning of the wavelengths of visible light, in blue region with dramatic decrease in yellow-red regions. Additional information about the spectral function, such as its minimum, maximum and gradient were saved as well in the catalogue. This information can supplement the analysis and help us decide which material the spectrum corresponds to even if the similarity percentage is low. However detailed analysis is still underway, with option to study separate regions of wavelengths instead of the spectral function as a whole.

These three groups conclude the three major categories of spectral data we are looking for. The fact that AMOS spectral cameras are capable of recording these three specific types of spectra with distinct precision unravels the great capabilities within the AMOS system. The remaining data was divided into three major groups - aluminium prospects, MLI prospects and solar panel prospects. Because of the long spanned time period, and repetitive appearance of some satellites, ageing and space weathering effects will be studied in detail in the future. However drawing conclusions and cataloguing such a vast majority of data will require a deeper study which is not within the scope of this paper.

5. SPECTRUM TRANSFORMATION INTO THE BVRI DIAGRAM

The re-connection of the high-resolution reflectance spectroscopy and the BVRI photometry offers for both methods additional data for the calibration and methods for the interpretation of the results. The transformation of the spectra into the color indices represents in other words the blurring process of the data from high to lower resolution. Mathematically it requires the convolution of the spectrum and the spectral transmission of the photometric filters (Figure 12) and estimation of the coefficients, which will be used for the calibration into the standard Johnson/Cousin's system of magnitudes.

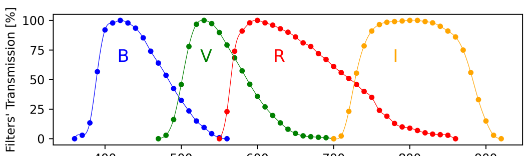

Figure 12: Spectral transmission of the Johnson/Cousin's photometric filters. Credit: [20]

The transformation is based on the general definition of the Johnson/Coussin's photometric system, which is defined by the spectrum of Vega. This star represents the zero magnitude in each passband. To be able to transform the normalized spectra from the Section 4, the high-resolution spectrum of the Vega from [21] was used to estimated the zero-point coefficients for each passband.

The spectrum was firstly normalized and convoluted with the filters' transmission (Figure 13). Afterwards, we integrated the area enclosed by the resulting curve and converted it into the magnitude logarithmic scale. Resulting magnitudes represent the transformation coefficients into the standard photometric system of magnitudes, thanks to the fact that Vega shall have zero magnitude in each passband.

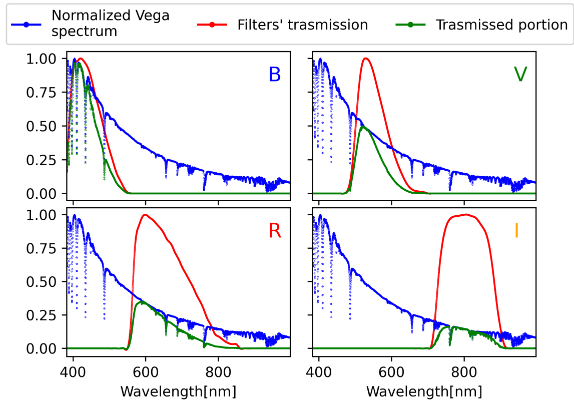

Figure 13: Normalized Vega spectrum from the [21] plotted along side with the filters' transmission and convoluted curves.

For the first calibration and to check, whether our approach results into the reasonable color indices, we transform the solar spectrum [18]. The process is the same as in the case of Vega spectrum except for the last step, when the resulting solar color indices were converted into the standard system using the zero-point coefficients. Results were confronted with the article [22] and can be seen in Table 2:

Table 2: Comparison of the resulting solar color indices with the [22]

Color index	Ramirez et al.	Our
B-V	0.653	0.635
V-R	0.356	0.375
V-I	0.701	0.736

The color indices of space debris represents the reflected sunlight affected by the target's surface characteristics. Because of this fact the deconvolution of the solar spectrum has to be omitted during spectrum calibration process and the reflectance spectra, which still contain the Sun's irradiation are transformed. Therefore, the spectra are convoluted with the filter's transmission, integrated, calibrated with the zero-point coefficients. To avoid any extrapolation, for the whole process we used the shortest wavelength interval from the whole data-set, which is the interval of the AMOS-Spec camera. Converted were the spectra related to objects SPOT 3 (93061A, 22823) and Iridium 44 (97077B., 25078). Additionally, we transformed the laboratory measured spectra of the gold MLI, aluminium and solar cell from the [19].

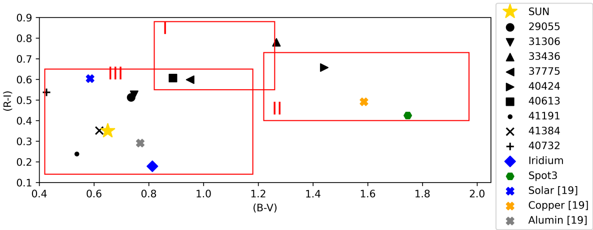

Figure 14: Resulting color indices after the transformation in comparison with the standard indices of the selected GEO satellites and laboratory measured materials and material groups.

In the Figure 14, can be seen the averaged color indices of stable GEO satellites plotted along with the reference blocks from [10]. Both selected and transformed objects fit into the expected categories. The strongly reflective aluminized Iridium 44 (blue diamond) lies in the III category near the Sun and SPOT3 (green hexagon) satellite, with dominant reflection pushed to the red region, lies in the gold category II. We also transformed the example laboratory spectra into the color indices, which fit well except for the solar cell spectrum. This can be caused by the fact that [10] uses solar cell with strongly different spectrum for the definition of the category I as was used in [19]. The general uncertainty of the position in the BVRI plane is caused by the fact that the spectral response of the AMOS-spec camera has shorter wavelength interval than general definition of the Johnson/Cousin's filters. This causes the loss of intensity in the marginal B and I passbands. It has to be taken to account during the interpretation of the results as a hardware limitation of the system.

6. CONCLUSIONS

In this work we presented the methodology of the color index extraction from the photometric data acquired by the AGO70 telescope and calibration of the spectra from the AMOS-Spec cameras originally designed for the meteor's spectra. Our work indicates that with our instruments and rigorous approach great deal of information can be extracted from the color indices and reflectance spectra of different artificial objects. However, the object characterization through the low as well as high resolution spectroscopic methods, requires extensively sensitive analysis and high data quality. Even small deviations in the input data can strongly influence the results and lead to the miss interpretations. Therefore, each of the above mentioned techniques will be further investigated and validated.

The combination of these methods can provide us with more complex view of the different populations and can be used as the cross-validation of both techniques. The spectra from the AMOS-Spec camera will extend our catalog of the color indices, which can be used for the observation planning and further identification of the space debris objects' surface characteristics.

ACKNOWLEDGMENTS

This work has been supported by the grant for PhD students and young researchers at Comenius University in Bratislava, Slovakia with project number UK/247/2020, Slovak Research and Development Agency grant APVV-16-0148 and grant of Ministry of Education, Science, Research and Sport of the Slovak Republic with number VEGA 1/0596/18.

REFERENCES

1. Šilha J. et al., (2021) Development and operational status of AGO70 telescope, In proceedings of *8th European Conference on Space Debris*, Darmstadt, Germany
2. Šilha J. et al., (2020) Space debris observations with the Slovak AGO70 telescope: Astrometry and light curves. In *Advances in Space Research*,65(8):2018–2035
3. Tóth J. et al., (2015) All-sky Meteor Orbit System AMOS and preliminary analysis of three unusual meteor showers. In *Planetary and Space Science*, 118: 102-106
4. Matlovič P. et al., (2020) Characterization of the June epsilon Ophiuchids meteoroidstream and the comet 300P/Catalina. In *Astronomy and Astrophysics* 636, A122
5. Žilková D. et al. (2019) Applications of AMOS meteor all-sky detection system for space debris research. In proceedings of *1st international orbital debris conference*, Houston, USA
6. Zigo M. et al. (2019) BVRI photometry of space debris objects at the AGO in Modra. In Proceedings of *Advanced Maui Optical and Space Surveillance Technologies Conference*, Hawaii, USA
7. Arlo U Landolt, (1992) Ubvri photometric standard stars in the magnitude range 11.5-16.0around the celestial equator. In *The Astronomical Journal*, 104:340–371
8. Arlo U Landolt, (2009) Ubvri photometric standard stars around the celestial equator:updates and additions. In *The Astronomical Journal*, 137(5):4186
9. Merline, W. J., Howell, S. B. (1995). A realistic model for point-sources imaged on array detectors: The model and initial results. In *Experimental Astronomy*, 6(1-2), 163-210.
10. Vananti, A., Schildknecht, T., & Krag, H. (2017). Reflectance spectroscopy characterization of space debris. in *Advances in space research*, 59(10), 2488-2500.
11. Popescu M., (2012) Techniques for asteroid spectroscopy. In *Earth and Planetary Astrophysics [astroph.EP]*. Observatoire de Paris; Universitatea Politehnica din Bucuresti, Facultatea de Ştiinţe Aplicate

12. ImageJ (2020) Image Processing and Analysis in Java *https://imagej.nih.gov/ij/index.html*

13. SonotaCo (2019) UFOAnalyzerV2, V2.48 *http://sonotaco.com/soft/e_index.html*

14. Šilha et al. (2019) AGO70 Telescope, Slovak Optical System for Space Debris Research, Surveillance and SLR Tracking Support. In Proceedings of the *1st Orbital Debris Conference*, Houston, USA

15. D. A. Vallado and P. Crawford and R. Hujsak and T. S. Kelso (2006) Revisiting spacetrack report 3. In Proceedings of *The AIAAAAS Astrodynamics Specialist Conference.* M.S., University of Colorado, Boulder. American Institute of Aeronautics and Astronautics

16. SIAC, United States Special Operations Command, *www.space-track.org*

17. AERIS/CNRS (2012-2020) Transmissions Atmosphériques Personnalisées Pour l'AStronomie *http://cds-espri.ipsl.fr/tapas/data?methodName=viewForm*

18. LLC (2020) NREL Transforming Energy, 2000 ASTM Standard Extraterrestrial Spectrum Reference E-490-00. *https://www.nrel.gov/grid/solar-resource/spectra-astm-e490.html*

19. Abercromby K. et al., (2013) Comparisons of a constrained least squares model versus human-in-the-loop for spectral unmixing to determine material type of geo debris. In Proceedings of the *6th European Conference on Space Debris*, Darmstadt, Germany

20. Bessell, M. S. (2005). Standard photometric systems. In *Annu. Rev. Astron. Astrophys.*, 43, 293-336.

21. Takeda, Y., Kawanomoto, S., Ohishi, N. (2007). High-resolution and high-S/N spectrum atlas of Vega. In *Publications of the Astronomical Society of Japan*, 59(1), 245-261.

22. Ramírez, I. et al. (2012) The ubv (ri) c colors of the sun. In *The Astrophysical Journal*, 752(1), 5.